

Automated Image Analysis Methods for 3-D Quantification of the Neurovascular Unit from Multi-Channel Confocal Microscope Images[#]

G Lin^{*,1}, CS Bjornsson^{†,2}, KL Smith[‡], MA Abdul-Karim^{*}, JN Turner[‡], W Shain[‡], B Roysam^{*}

^{*}Department of Electrical, Computer, and Systems Engineering,

Rensselaer Polytechnic Institute, Troy, NY 12180-3590

[‡]Laboratory of Nervous System Disorders,

New York State Department of Health, Wadsworth Center, Albany, NY 12201-0509

ABSTRACT

Background: There is a need for integrative and quantitative methods to investigate the structural and functional relationships among elements of complex systems such as the neurovascular unit (NVU) that involve multiple cell types, microvasculature, and various genomic/proteomic/ionic functional entities.

Methods: Vascular casting and selective labeling enabled simultaneous 3-D imaging of the microvasculature, cell nuclei, and cytoplasmic stains. Multi-dimensional segmentation was achieved by: (i) bleed-through removal and attenuation correction; (ii) independent segmentation and morphometry for each corrected channel; and (iii) spatially-associative feature computation across channels. The combined measurements enable cell classification based on nuclear morphometry, cytoplasmic signals, and distance from vascular elements. Specific spatial relationships among the NVU elements can be quantified.

Results: A software system combining nuclear and vessel segmentation codes, and associative features was constructed and validated. Biological variability contributed to misidentified nuclei (9.3%), undersegmentation (3.7%), hypersegmentation (14%) of nuclei, and missed nuclei (4.7%). Microvessel segmentation errors occurred rarely, mainly due to non-uniform lumen staining.

Conclusions: Associative features across fluorescence channels, in combination with standard features, enable integrative structural and functional analysis of the NVU. By labeling additional structural and functional entities, this method can be scaled up to larger-scale systems biology studies that integrate spatial and molecular information.

Key terms: Multi-dimensional image analysis, 3-D Blob segmentation, 3-D microvessel tracing, object features, inter-object features, confocal microscopy, vascular casting, neurovascular unit.

Correspondence: Badrinath Roysam, Professor, JEC 7010, Rensselaer Polytechnic Institute, Troy, NY 12180-3590, USA. **Phone:** 518-276-8067, **Fax:** 518-276-8715, roysam@ecse.rpi.edu

[#] The Rensselaer portion of this work was supported in parts by the Center for Subsurface Sensing and Imaging Systems, under the NSF Engineering Research Centers Program (EEC-9986821), and NIH grants AG18230, and AG023309. The Wadsworth portion of this work was supported in part by NIH grants NIBIB R01-EB000359, and NINDS R01-NS1044287.

^{1,2} These authors have contributed equally.

1. INTRODUCTION

The structural and functional complexity of the nervous system is monumental. At the cellular level, neurons and supporting glia are intimately linked to the neurovasculature that supports them – increased neuronal activity places greater demands on the circulatory system and increases local cerebral blood flow by regulating vascular tone (functional hyperemia) (Park *et al.* 2003; Zonta *et al.* 2003). The neurovasculature can influence neuronal function as well, especially in response to injury through coordinated release of neuroangiogenic factors (del Zoppo 1994; Yoder 2002; Park *et al.* 2003). Astrocytes mediate many of these interactions (Simard *et al.* 2003; Zonta *et al.* 2003). In many cortical regions the vascular architecture recapitulates the underlying neural organization (Cox *et al.* 1993; Woolsey *et al.* 1996). The organization and interplay between neurons, glia, and blood vessels have fostered the concept of the neurovascular unit (NVU) as a distinctive structural and functional entity within the CNS that is worthy of study in its own right (del Zoppo 1994; del Zoppo and Mabuchi 2003; Park *et al.* 2003).

A quantitative structural elucidation of NVU necessarily requires three-dimensional (3-D) imaging to describe the structures of the individual NVU elements, as well as their relative spatial juxtaposition and organization. A complete functional elucidation of the NVU requires some form of molecular imaging in order to map the presence and spatial distribution of various functional genomic and proteomic markers. All of this must be done with subcellular resolution. These considerations motivate the use of modern optical microscopy as the investigative tool of choice.

Contemporary techniques allow selective fluorescent labeling of multiple structural and functional entities within the NVU. This, when combined with multi-spectral confocal/multi-photon microscopy provides the opportunity to generate detailed as well as extensive 3-D imagery of these entities in a manner that preserves their anatomic characteristics, as well as important spatial relationships among them. Thick tissue samples containing multiple labeled cell types can be used to study how the organization of the NVU varies between cortical layers and brain regions and to investigate NVU changes associated with disease and injury. From a systems biology perspective (Kitano 2002), modern

microscopy is valuable for its ability to record structures and functional markers in intact tissue while avoiding the need to fragment cells through preparation of thin tissue sections. Spatial distributions and interactions among multiple structural and functional markers in intact tissue are preserved unlike biochemical assays, gene arrays (Kohane *et al.* 2003) and flow cytometry (Shapiro 2003), in which spatial information is inevitably disrupted. While these methods do provide temporal data, they do not relate it with spatial information. On a practical basis, imaging is also attractive for its intuitive visual confirmation capability. Overall, image-based approaches to investigating the NVU offer key advantages, and a complement to other strategies.

Recently, there has been an explosive growth in the sophistication of optical microscopy (Pawley 1995; Sheppard *et al.* 1997; Diaspro 2002; Matsumoto and American Society for Cell 2002). Multi-spectral imaging, with its ability to disentangle overlapping fluorescent emissions, enables simultaneous observation of multiple labels, providing a wealth of molecular data (Dickinson *et al.* 2001; Zimmermann *et al.* 2002; Zimmermann *et al.* 2003). Burgeoning fluorophore libraries now permit ever larger numbers of highly-specific structural and functional entities (genomic, proteomic, and ionic, among others) to be labeled simultaneously (Valeur 2002; Zimmermann *et al.* 2003). With the widespread availability of axially-resolved imaging techniques, notably confocal and multi-photon microscopy, 3-D imaging is now routine. With the advent of technologies for handling time-resolved, 3-D imaging of live specimens, there is reason to be optimistic about the future of optical microscopy in elucidating the NVU. In the future, such analyses can also be expected to be possible on a large scale using seamless large-field high-resolution imaging by automatic montaging (Becker *et al.* 1996; Beck *et al.* 2000; Al-Kofahi *et al.* 2002). In this paper, we use the term “multi-dimensional microscopy” to refer to the combination of spatial, temporal, and spectral dimensions accessible by modern microscopy.

While multi-dimensional imaging as noted above can provide a wealth of detailed and sophisticated data, it has remained difficult to translate this massive data into quantitative insight. Automated image analysis is the computational process of making quantitative structural and functional measurements from an image in a manner that avoids/minimizes subjective errors. The past decade has resulted in significant

progress in 3-D image analysis. For instance, rapid and automated segmentation of fluorescently-labeled blob-like structures such as cell nuclei, and quantitation of various genomic signals relative to this segmentation is now a mature and routinely used technology (Lin *et al.* 2003; Chawla *et al.* 2004; Lin *et al.* 2004). Rapid, accurate and robust 3-D tracing and morphometry of tube-like structures such as neuronal processes and microvasculature have matured separately to a level that they can be employed routinely (Cohen *et al.* 1994; Can *et al.* 1999; Al-Kofahi *et al.* 2002; Can *et al.* 2002; Abdul-Karim *et al.* 2003; He *et al.* 2003). At the very least, the automated methods described here can enable a major reduction in tedium and manual effort ordinarily associated with image analysis. At a higher level, they offer several advantages over manual analysis, including the handling of high-dimensional data, speed, consistency, quantitative accuracy, and the capability to query complex spatial databases.

The goal of this work is to demonstrate the practical feasibility of extending and integrating these prior advances in a manner that addresses the needs posed by complex systems such as the NVU. *The main idea is to identify, and quantify the associations between spatial and functional entities revealed by various fluorophores in a manner that is insightful yet practically feasible.* Specifically, segmentations of objects such as cell nuclei and the microvasculature can be thought of as local structural references, or “spatial anchors” relative to which a multitude of fluorescent markers can be readily associated and mapped. Furthermore, with imaging, it becomes possible to link the molecule-specific information available from fluorescence microscopy with conventional image cytometric measurements such as nuclear size, shape, and texture, to derive additional quantitative descriptions that cannot be generated by either approach individually. The end result of the analysis described here is a multi-dimensional tabular morphometric summary, that can be stored in database form, or spreadsheets for graphing, query, and further quantitative analysis. We provide illustrative examples of such analysis.

2. MATERIALS AND METHODS

Specimen Preparation and Imaging

Laser scanning confocal microscopy was used to collect 3-D images of triple-labeled brain tissue slices highlighting three key constituents of the NVU: the microvasculature, cell nuclei, and Nissl

substance. The microvasculature was filled using a vascular casting protocol described below. A nucleic acid stain was used to label nuclei of all cells, including neurons, endothelial cells, astrocytes, microglia, oligodendrocytes, smooth muscle cells, and pericytes. Two possible approaches to distinguish among these cell types include: (i) use of a distinguishing cytoplasmic stain; and (ii) use of morphometric data for the nuclei, such as shape, texture, size, and spatial location relative to the microvasculature. We used Nissl staining to illustrate the former approach, and describe how these two can be combined in the next section. The use of Nissl staining is just one example of the potential of this technique to highlight different elements of the neurovascular unit.

Male Sprague-Dawley rats (Taconic Farms, NY) were housed at standard temperature in a light-controlled environment, with *ad libitum* access to food and water. All protocols were approved by the International Animal Care and Use Committee (IACUC) of the Wadsworth center. Animals weighing 100-130 g were anesthetized with tribromoethanol (23mg/100g body weight), and transcardially perfused using a constant-pressure perfusion apparatus (Olson 1985), which allowed us to record perfusion pressure and flow rate. 200 ml heparinized (1U/ml) isotonic buffer (200 ml) was perfused through the ascending aorta at 200 mm Hg, before fixation with 200 ml 4% paraformaldehyde in phosphate buffer at 110-130 mm Hg. The elevated buffer pressure was essential to achieve adequate fixation. We recorded flow rates for buffer between 110-130 ml/min, and fixative flow rates between 50-75 ml/min. During fixation, a premixed solution consisting of 40 ml Mercor-B (Ladd Research, Inc, VT), 10 ml methyl methacrylate (Fluka), and 15 mg Rhodamine B (Sigma-Aldrich, St. Louis, MO) was added to 0.8 ml catalyst (Ladd Research, Inc, VT) and poured into a 60 ml syringe casing to prepare the fluorescent casting resin (Castenholz 1995). A rubber stopper fitted with ports connected to a rubber bulb and a sphygmomanometer was placed over the back of the syringe casing, and the spout was connected to the perfusion needle. Mercor was injected at 200-300 mm Hg, and left to polymerize for 30 minutes before brains were harvested. Mercor-injected brains were allowed to polymerize further at 37°C for 3-4 hours in 4% paraformaldehyde before storage overnight at 4°C. After 24h, the brain was washed in PBS. Slices approximately 1 mm thick were cut by hand with a fresh razor blade. Brain slices were permeabilized in

0.2% Triton X-100 in HEPES-buffered Hanks (HBHS) for 30 minutes, washed in HBHS, and stained overnight using CyQuant (1:1000; Molecular Probes, Eugene, OR) and NeuroTrace (1:125; Molecular Probes). Slices were then washed and mounted in HBHS.

Images were collected using a NORAN laser scanning confocal attachment and an Olympus IX-70 microscope fitted with a 40xW/1.2NA objective. Z-series image stacks were collected using 1.0 μm steps. Photomultiplier gain and black level settings were optimized for each image separately to achieve the optimal dynamic range. Figure 1 shows a maximum projection display of a representative 3-color 3-D confocal microscope image stack, as part of a screen view of the integrative software system. The cell nuclei (blobs) are displayed in green. Blood vessels (tubes) are displayed in red, and the unstructured cloud-like Nissl cytoplasmic stain is displayed in blue. Three distinctive blob morphologies can be observed in the data: larger, dimmer, and more heterogeneous neuronal nuclei; smaller, brighter and more uniform glia; and flat, intense endothelial cells. Differences in cloud shape and volume can also be used to distinguish larger pyramidal neurons from other neuron types. Figure 2 summarizes the main procedures for automated analysis of these 3-D image stacks containing different types of object. The detailed process of analyzing datasets such as this are described below.

Image Pre-Processing

The effects of common imaging artifacts include bleed-through of signals between imaging channels, intensity non-uniformity in x , y and z , and presence of uninteresting/confounding objects. The bleed-through elimination used in this work was based on simple subtraction. Sometimes, non-uniform illumination causes different parts of the image to exhibit different contrast or brightness. Alternatively, foreground objects may appear grainy. Figure 3 illustrates several imaging artifacts, which must be eliminated using a pre-processing step.

Median filtering, morphological operations (Serra and Soille 1994; Bovik *et al.* 2001), background subtraction (Russ 1994), and signal attenuation-correction (Adiga and Chaudhuri 2001; Can *et al.* 2003) are examples of common preprocessing methods. Median filtering can be used to remove the shot noise

of the image. Morphological filters, such as open/close and top-hat filter, are typically utilized to remove noise and smooth out non-uniformities of foreground intensity, such as holes inside objects and small island-like artifacts. Background subtraction is performed to correct illumination non-uniformity across the entire image. Signal attenuation-correction is useful to rectify depth-dependent attenuation of signals (Can *et al.* 2003).

Another rationale to preprocessing is to generate “standardized images” where one segmentation method is used for images coming from different sources. For example, images of a similar biological object from different experiments may exhibit different contrast and illumination characteristics, requiring them to be “standardized” prior to segmentation. At the other extreme, images of neuronal processes and vasculature may be preprocessed to accentuate the tube-like morphology of these biological objects (Sato *et al.* 1998).

Note that many of neuronal nuclei are very distinct in our images, as shown in green in Figure 3. These cells possess large nuclei with prominent nucleoli and a clear ring of heterochromatin associated with the nuclear lamina. The euchromatin occupying most of the nuclear volume takes on very little stain, making these nuclei appear much dimmer than the surrounding glia and endothelial cells. In addition, crosstalk was observed between the Cy5 (Nissl) channel and the CyQuant (nuclei) channel around these neurons in some images. Therefore, the following special pre-processing steps were needed: The Cy5 (Nissl) channel was detected and then subtracted from the nuclei channel to eliminate bleed-through. The interior region of the rings around dim nuclei was masked out in order to be extracted using lower foreground threshold during the subsequent segmentation.

Segmentation Methods

Segmentation is the process of identifying and delineating “objects” in the image data, which is the critical first step in our image analysis. The main objects of interest in the NVU include the microvasculature, the cell nuclei, and various genomic or proteomic markers. The microvasculature is representative of a broader class of image objects referred to in the image analysis literature as “tubes”.

The cell nuclei are similarly representative of “blobs” while the Nissl bodies appear as “clouds”. Another type of object that does not appear in our examples, but is nevertheless relevant to the NVU is genomic/proteomic “foci” or punctae (Netten *et al.* 1997; Solórzano *et al.* 1998; Adiga and Chaudhuri 1999; Castleman and White 2001; Chawla *et al.* 2004). The specimen preparation and imaging procedure outlined above provides a powerful form of simplification and extensibility: each of the fluorescent channels is “pure” in the sense that it contains only one type of object. This greatly simplifies the image analysis task.

An integrated and extensible software package, termed FARSIGHT (Fluorescence Association Rules for Quantitative Insight) was developed that combines several separately developed packages, especially blob segmentation and FISH quantitation (Chawla *et al.* 2004), and tube segmentation (Abdul-Karim *et al.* 2003) under a common software platform provided by IDL (Interactive Data Language, Research Systems, Boulder, CO). Figure 1 shows a screen view of this integrative software package.

Nuclear channel segmentation: The fluorescently labeled cell nuclei (green channel) in Figure 1 are examples of 3-D blobs, by far the most common type of object of interest in automated image analysis. These apparently simple objects nevertheless provide a rich set of challenges from the standpoint of automated image analysis (Lin *et al.* 2003).

The prior literature describes two main approaches to blob segmentation: top-down and bottom-up methods. Top-down segmentation is guided by some *a priori* knowledge of the morphology of objects in question, such as expected object volumes and shapes (Sunil Kumar and Desai 1999; Neumann 2003). Bottom-up approaches start with an over-segmentation of the image and iteratively merge regions based on some measure of similarity (Zucker 1976); (Besl and Jain 1988; Adams and Bischof 1994; Trucco and Fisher 1995; Zhu and Yuille 1996). Some methods operate iteratively by grouping together neighboring voxels that have similar features (Blake and Zisserman 1987; Black and Rangarajan 1996) and graph-based clustering (Xu and Uberbacher 1997; Shi and Malik 2000; Guigues *et al.* 2003), and splitting groups of voxels that are dissimilar, such as widely used watershed algorithm (Vincent and Soille 1991) (Ancin *et al.* 1996) (Malpica *et al.* 1997) (Adiga and Chaudhuri 2001) (Solórzano and Rodríguez 1999).

As revealed in the green channel in Figure 1, tightly packed cell layers, which often result in the appearance of “touching objects” in the image stacks present the main segmentation challenge. Lin et al. (Lin *et al.* 2003) described an improved algorithm using two ideas: (i) a distance transform combining intensity gradients and geometric distance for the watershed object separation step; and (ii) deliberate initial over-segmentation, followed by statistical model-based merging. In (Lin *et al.* 2004), a more accurate recursive tree-based algorithm that can consider multiple object fragments simultaneously for the merging. The main ideas behind these methods are summarized below.

The watershed algorithm is widely used for efficient connected object separation (Vincent and Soille 1991; Ancin *et al.* 1996; Malpica *et al.* 1997; Solorzano and Rodriguez 1999). It’s main limitations arise from the fact that it relies on touching objects exhibiting an often unreliable “neck” in the region of contact. Considerable effort has been devoted to the design of algorithms for generating the correct set of “geometric markers” to guide the object segmentation. To overcome this challenge, Lin et al. proposed (Lin *et al.* 2003) a “gradient-weighted distance transform”, that combines object separation hints derived from geometric and intensity cues in the image data. Specifically, the geometric-distance transform \mathbf{D} (Borgefors 1986), and the gradient transform \mathbf{G} (Lin *et al.* 2003) are combined into a single representation that captures the object separation cues available in the data, as given by the following formula.

$$\mathbf{D}' = \mathbf{D} \times \exp \left(1 - \frac{\mathbf{G} - G_{\min}}{G_{\max} - G_{\min}} \right), \quad (1)$$

where G_{\min} and G_{\max} are the minimum and maximum values of the gradient \mathbf{G} needed for normalization. This expresses the object separation cue that the voxels with bigger gradient values tend to lie on the boundary of an object. In practice, the watershed algorithm requires the inverse of this distance transformation. This inverse is denoted \mathbf{T} , and is computed as follows:

$$\mathbf{T} = S_g (\max(\mathbf{D}') - \mathbf{D}'), \quad (2)$$

where $\max(\mathbf{D}')$ is the global maximum within the distance images, and S_g represents a Gaussian smoothing operator (Castleman 1996) to overcome uneven cell staining. This combined transformation is

effective in discriminating touching nuclear clusters even when they do not exhibit the characteristic bottleneck-shaped pattern.

To correct the still remnant over-segmentation after the above watershed segmentation, it is necessary to detect and break (eliminate) false watershed surfaces and thereby merge the objects (Adiga and Chaudhuri 2001; Lin *et al.* 2003). Currently, the best methods rely on a quantitative mathematical model of the objects of interest (i.e., the nuclei) that is described by a vector of features, denoted X_c , and including the volume, texture, convexity, circularity and shape. The merging score based on these features assuming that they are Gaussian distributed is given by:

$$S_c = p(X_c) = \frac{1}{(2\pi)^{m/2} |\Sigma_X|^{1/2}} \exp\left(-\frac{1}{2} \sqrt{(X_c - \bar{X})^T \Sigma_X^{-1} (X_c - \bar{X})}\right), \quad (3)$$

where \bar{X} and Σ_X are the mean and covariance matrix of the training feature set respectively, which are obtained from some example intact nuclei in the given image stack.

Intuitively, the merging decisions can be based on the following two criteria: (i) the merging score S_{c_w} , i.e., the score of the combined object by nucleus c_w^1 , c_w^2 and watershed surface w , should be higher than the score of either nucleus $S_{c_w^1}$ or $S_{c_w^2}$ before merging. (ii) The gradient of watershed surface w should be relatively large compared with the gradient of nucleus c_w^1 and c_w^2 . This is based on assuming that intra-nuclear gradients are smaller than inter-nuclear gradients, which generally holds true. The final decision making criterion is of the following form:

$$\frac{2 \times S_{c_w}}{(S_{c_w^1} + S_{c_w^2})} \times \frac{(\gamma_{c_w^1} + \gamma_{c_w^2})}{2 \times \gamma_w} \geq \beta \quad (4)$$

where β is an empirically set decision threshold. This model-based merging method effectively eliminates most of the over-segmented objects by initial watershed segmentation (Lin *et al.* 2003). For cases of severe over-segmentation, we have described a further improved hierarchical method for performing the merging decisions taking into account multiple connected fragments at a time, relying on a

region adjacency graph (Ballard and Brown 1982; Wu 1993; Lin *et al.* 2004) constructed from the object fragments.

Segmentation of the Microvasculature: Vasculature (red channel in Figure 1) and neuronal processes are instances of tubes, which are non-uniformly deformed 3-D cylinders (Al-Kofahi *et al.* 2002; Abdul-Karim *et al.* 2003). Like blobs, these objects provide a rich set of challenges for automated image analysis systems. Tube-like objects can be filled (i.e., solid) (Al-Kofahi *et al.* 2002; Abdul-Karim *et al.* 2003; He *et al.* 2003; Meijering *et al.* 2004) or hollow (Weichert *et al.* 2003) in appearance. If more than one appearance model exists, robust model-fitting algorithm can be used (Mahadevan *et al.* 2004).

Two types of algorithms exist for segmenting tube-like objects: skeletonization and vectorization. Skeletonization methods work by eroding a binarized version of the image until only the innermost skeleton remains, and are attractive when the objects are irregular, for instance, spiny neurons (Koh *et al.* 2002). Vectorization methods are appropriate when the objects are well modeled as generalized cylinders (Al-Kofahi *et al.* 2002; Abdul-Karim *et al.* 2003). This method exploits more structural assumptions to better reject image clutter compared to skeletonization based methods.

For the data of interest, the strict cylinder model is relaxed to account for slight irregularities in the vasculature boundaries by incorporating a tolerance to deviations from the strict cylinder model in the software implementation. Often, the microvasculature is irregular. This irregularity can be modeled by the use of robust statistics (Abdul-Karim *et al.* 2003). This method is summarized below, and illustrated diagrammatically in Figure 4.

At the core of this method is the estimation of vessel boundary locations and centerlines using a set of robust edge detectors (Sun *et al.* 1995) (Al-Kofahi *et al.* 2002) (Abdul-Karim *et al.* 2003) that allow sequential tracing along a vessel, starting from an initial guess that is automatically generated. Due to intensity variations within the vasculature (e.g., as in Figure 2), our previous method of using local 1-D maxima along rectangular grid overlaid on the image as initial guesses (Al-Kofahi *et al.* 2002) proved unsatisfactory. This prompted us to formulate the initial guesses as a vessel detection problem in 1-D

using a modified robust matched-filtering method (Kay 1993). Following seed detection, the core tracing algorithm proceeds by an update equation of the following form:

$$(\mathbf{b}^i, \mathbf{u}^i, k^i) = \arg \max_{\{(\mathbf{b}, \mathbf{u}, k) \mid \mathbf{b} = \mathbf{p}^i + m\mathbf{u}_\perp, m=1, \dots, \frac{M}{2}, \mathbf{u} \in \mathbf{U}, k \in K\}} \left\{ R(\mathbf{b}, \mathbf{u}, K) \right\}, \quad (5)$$

where \mathbf{U} is the set of unit vectors along directions in the neighborhood of \mathbf{u}^i and K is the set of all template lengths. The vector \mathbf{u} is a unit vector along a particular 3-D angle θ . while \mathbf{u}_\perp is the unit vector perpendicular to \mathbf{u} . The parameter M is the user-defined diameter of the widest expected vasculature. Values $(\mathbf{b}^i, \mathbf{u}^i, k^i)$ are the results of this exhaustive search at iteration i , each representing the $[x \ y \ z]$ location, orientation, and length respectively of the template that returns the maximum response R . This search is performed four times corresponding to the four templates that make up the generalized cylinder model (Figure 4). The corresponding template response is expressed as

$$R(\mathbf{b}, \mathbf{u}, K) = \arg \max_{k \in K} \left\{ \text{median}_{j=1..k} (r(\mathbf{b} + j\mathbf{u}, \mathbf{u}_\perp)) \right\}, \quad (6)$$

where $r(\mathbf{b}, \mathbf{u}_\perp)$ is the response of a single 1-D edge detector at \mathbf{b} along the direction \mathbf{u}_\perp that is perpendicular to \mathbf{u} . Notice that a template of length k is comprised of k 1-D edge detectors stacked together, hence, r is essentially a template of length 1. By using the median, the response function is robust to at most 50% of outliers (Huber 1981), loosely-termed as *bad edges*. Overall, this method essentially performs edge detection perpendicular to the object, and averages the edge-strengths along the object boundary.

Notice that by using this method, in addition to the centerline and boundary locations, morphometric data such as length (cumulative distance between center points) and diameter (distance between boundary points) are obtained as the tracing progresses. Details are described elsewhere (Al-Kofahi *et al.* 2002; Abdul-Karim *et al.* 2003).

Segmentation of Nissl clouds: The diffuse cytoplasmic (Nissl) stain shown in blue channel of Figure 1 is a good example of this class of object (Lin *et al.* 2003). The ability of these objects to provide information detailing cellular and molecular structure and function, coupled with the diversity of available

fluorophores and the ability of modern confocal microscopes to image multiple fluorophores, makes this an important and rapidly growing category of image analysis targets. Although these objects do not always have clear-cut geometric descriptions, they are often amenable to segmentation and quantitation by spatial association with biologically related blob-like or tube-like objects. To segment these cloud-like regions, we simply extracted the foreground by intensity thresholding after the pre-processing, followed by morphological opening and closing, and connected component analysis to delineate the individual objects. The detected objects will be associated with the cell nuclei, which is described next.

Individual and Inter-Object Feature Computation by Association

Once the microvascular tubes, nuclear blobs, and Nissl clouds are segmented from the separate channels as described above, it becomes possible to quantify the relationships between these three-different types of objects in a biologically informative manner. The methods are described below.

Nuclear Feature Calculation: Once segmented as described above, a wealth of nuclear morphometric data become available, including the 3-D centroidal coordinates, average intensity, volume, texture and shape factor, etc. Table 1 shows a fragment of such a morphometric summary that is routinely generated by the blob segmentation software described in prior work (Lin *et al.* 2003; Chawla *et al.* 2004; Lin *et al.* 2004). Given the non-stoichiometric nature of the dyes used, the absence of calibration targets, and depth-dependent attenuation, we emphasize the use of measurements of spatial factors over the fluorescent intensity values. If the fluorescence signal can be made quantitative, these features can also be exploited in a direct manner.

The size and shape of the nuclei allow further discrimination of cell types. The nuclear volume is the total number of voxels in a segmented nucleus. The shape factor measures how spherical an object (blob)

is, and defined mathematically as: $S = \frac{9 \times |\mathbf{b}|^3}{1024 \times \pi \times V^2}$, where \mathbf{b} denotes the surface voxels of an object,

and V is the volume of the object. Notice that S usually takes value between 0 and 1. The closer this number is to one, the closer the object is to a sphere. This feature can be used to distinguish the types of

nuclei in the image. For example, normal neurons tend to be spherical, and endothelial cells are more slim and elliptical.

Texture measurement reflects the uniformity of the chromatin, as reflected by the intensity of nuclear voxels. There are several ways to quantify texture. The simplest one is the variation of intensity value among all nuclear voxels, i.e., $T = \sigma(I(\mathbf{X}_o))$, where σ stands for the standard deviation operator, and \mathbf{X}_o denotes the intensity of the object voxels. The more sophisticated texture can be defined by the second order histogram of the intensity values (co-occurrence matrix). It is obviously more computationally intensive. We used the first method after attenuation correction of the nuclear channel.

Vascular Feature Computation: Although a rich set of vascular measurements are collected by the tracing software during the tracing operations as described in the previous section, only the simplest of these were used in this work. These included the location of centerline points, and the boundary surface of the vessels, and local widths and direction vectors at each of the centerline points.

Associations between the nuclei and the Nissl cytoplasmic stain: In analyzing the nuclear (CyQuant) data we were interested in being able to distinguish neurons and endothelial cells on the basis of their morphology and proximity to Nissl substance (clouds) or neurovasculature (tubes), respectively. The cellular diversity encountered in the rat neocortex produced a range of nuclear profiles with marked differences in morphology and staining intensity. Preliminary assessment of the neuronal count indicated that many highly active neuronal nuclei displaying poor, heterogeneous CyQuant labeling were not detected by the software, even when the threshold was set so low that false positives (artifacts) were being counted.

From a software analysis standpoint, the Nissl clouds essentially surround the nuclei, or exist in close proximity. Each voxel in the Nissl cloud was associated with the nearest nucleus based on its Euclidean distance from the nuclear surface (Chawla *et al.* 2004). This allows the nuclei in the image to be classified into two broad categories based on whether or not they are associated with the Nissl stain. Specifically, if the total intensity of Nissl signals in the region-of-interest (a shell with certain thickness surrounding nucleus) exceeds a pre-specified threshold, we deem the nucleus as Nissl-positive, thus the corresponding

cell is a neuron. An unavoidable challenge, noted above, is the differential attenuation of the Nissl stain compared to the nuclear Cyquant stain. In general, a more rapid attenuation of the nuclear stain compared to the cytoplasmic stain results in invisible “ghost” nuclei that must be inferred from the missing part of the cytoplasmic stain. On the other hand, a more rapid attenuation of the cytoplasmic stain results in fewer detections of nuclei that are actually associated with the cytoplasmic stain. The depth-dependent attenuation correction and adaptive thresholding of the Nissl signal were helpful in minimizing such sources of error.

Associations between the nuclei and the microvasculature: Each nucleus was simply associated with the closest point on the vasculature as measured by its Euclidean distance from the centroid of the nucleus to the estimated surface of the vessel segment. Measuring the distance to the surface, as opposed to the centerline allows compensation for the variable thickness (bore) of the microvasculature, and also allows simple identification of cells that are closely associated with the microvasculature (e.g., endothelial cells). In addition, the distances of the cells from the microvasculature are biologically significant since the nutrient and oxygen levels of cells are directly affected by proximity to a microvessel. If the cell membrane is labeled separately, it is possible, in principle, to quantify its distance to the microvascular surface as well.

3. EXPERIMENTAL RESULTS

Manual Validation of the Image Analysis

The main objective of this analysis was to quantify the disagreement between automated and manually inspected results where a measurement of the disagreements is interpreted as the error. The manually inspected results have a large subjective component and, therefore, are prone to inter- and intra-observer variability. For blobs and clouds, errors include false detection (false positives), misses (false negatives), erroneous separation of connected objects (hypersegmentation), and errors in correctly delineating the boundaries of objects (Lin *et al.* 2003). In terms of classification, objects can be misidentified; in most cases this error can be reduced by careful evaluation, refinement and use of identifying criteria. For tube-like objects, errors include falsely traced segments and branch points (false

positives) and missed segments and branch points (false negatives), accuracy of the trace, accuracy of width measurements, and accuracy in locating branching/crossover points (Abu-Tarif and Ahmad 2002; Al-Kofahi *et al.* 2003).

Quantitative validation may also involve voxel-to-voxel comparisons of the segmented volume, or comparisons of any other entities derived from the segmented volume such as the vasculature centerline or the cell centroid. The comparison can be performed automatically to further reduce the subjectivity of validating the segmentation results (Al-Kofahi *et al.* 2002). In the case of tube-like objects, the centerline locations are extremely important since almost all morphometrics depend on them. Centerline locations are typically validated for the deviation from a “true” centerline, which reflects the accuracy of the automated method, and the centerline coverage of the objects in the image, which reflects how much manual editing the automated result needs.

Manual validation was performed on two datasets to confirm the accuracy of automated nuclear counting and neuronal and endothelial cell classification. Validation of automated categorization of cells was accomplished by manually reviewing the automated output of the 3-D datasets one optical section at a time. Neuronal nuclei were identified because of their close association with Nissl-stained clouds. Endothelial cell nuclei were identified by their nuclear morphology and close apposition to vascular elements in both 2-D projections and 3-D datasets. The “other cells” category includes all cells that did not meet either of the above criteria for categorization, and include astrocytes, microglia, oligodendrocytes, smooth muscle cells, and pericytes. In addition, cases of under- and hypersegmentation were scored. Erroneous boundary detection was not substantial except for a few instances where one object encroached on an immediately adjacent object, and therefore was not otherwise noted. In a representative dataset, the software identified 115 nuclei (blobs); 107 were detected through manual validation. Of these 107 nuclei, 5 (4.7%) were missed, 2 (1.9%) were involved in a substantial encroachment, 10 (9.3%) were hypersegmented to appear as 23 nuclei, and 4 (3.7%) were undersegmented to appear as 2 nuclei. Generally, the missed and hypersegmented nuclei had diffuse labeling: thus, these presented a serious challenge to the image analysis software. Most organs do not

display such a pronounced difference in nuclear morphology; indeed, nervous tissue, because of the variety of cells, e.g. large and small neurons, various glia, and endothelial cells, and testis, because of cells with different ploidy, e.g. Sertoli cells and developing spermatogonia, are among the most challenging tissues encountered in this regard.

Data are presented to describe measured distance between neuron, endothelial cell, and other cell nuclei and the edge of the nearest blood vessel (Fig. 6). Comparison of data from automatically categorized (Fig. 6A, C) and manually validated (Fig. 6B, D) nuclei demonstrates a high degree of accuracy and good agreement between the automated analysis and manual validation. In both datasets, the endothelia are easily distinguished by their location relative to the neurovasculature, while the neurons and other cells share a similar distribution. In the first data set (Fig. 6A, B) the mean distance of neurons from the nearest vessel is 13.3 μm (automated) or 14.7 μm (validated), while the mean distance of “other” cells is 16.6 μm (automated) or 15.9 μm (validated). Endothelial cell nuclei average $-0.4 \mu\text{m}$ (automated) or $-0.2 \mu\text{m}$ (validated) from the nearest vessel wall. In the second data set (Fig. 6C, D) the mean distance of neurons from the nearest vessel is 10.0 μm (automated) or 10.5 μm (validated), while the mean distance of “other” cells is 11.4 μm (automated) or 10.0 μm (validated). Endothelial cell nuclei average $-0.6 \mu\text{m}$ (automated) or $-0.1 \mu\text{m}$ (validated) from the nearest vessel wall. The differences between values for each dataset likely reflect differences in the organization of the NVU in different cortical regions.

Several cases of misidentification occurred when a neighboring glial cell was immediately adjacent to a neuron and was, therefore placed in the Nissl-positive category. By refining our criteria to require a greater percent area of blob-cloud interface, this error might be avoided. For instance, the nucleus could be scored as neuronal when a nucleus is almost completely surrounded by Nissl, while it would be scored as glial when contact with a Nissl boundary occurs over a small fraction of its own boundary. Misidentification errors can also be avoided through careful scrutiny of the data output by automated analysis and adjustment of criteria accordingly.

Figure 7 shows an example indicating the correlation of the distance between the calculated volume of each nucleus and its nearest neighboring vascular element for two datasets. Comparisons of

automatically identified nuclei (filled symbols) and validated observations (hollow symbols) demonstrate the accuracy of object detection. The primary source of error was hypersegmentation of nuclei, as indicated by several unvalidated smaller nuclei (e.g. numbered filled symbols). These smaller objects were manually grouped as indicated by the appearance of larger validated nuclei (e.g. numbered hollow symbol). Endothelial cells had some of the smallest nuclear volumes. Interestingly, neurons with larger nuclear volumes were only located further from vascular elements, while neurons with smaller nuclear volumes exhibited a more variable distribution. Other cell types (astrocytes, microglia, smooth muscle cells, pericytes) were also uniformly distributed; therefore, distinguishing these different cell populations will require additional techniques (Nissl staining, immunohistochemical labeling of specific glial markers, etc.). The distribution of astrocytes may result from their roles in blood-brain barrier function, in synaptic transmission, and metabolic support (Nedergaard *et al.* 2003; Newman 2003). In addition, microglia are likely to be uniformly dispersed throughout the cortex. Studies using additional histochemical or immunohistochemical markers to label astrocytes and microglia will further delineate the distribution of these cells and will provide functional information to define their roles in the neurovascular unit under normal and pathological conditions.

4. DISCUSSION AND CONCLUSIONS

We have presented a “divide and conquer” strategy for detailed and scalable analysis of complex biological systems using the neurovascular unit as example. Separately imaging multiple structural and functional entities in the system using multiple fluorescent markers together with innovative specimen preparation approaches results in a set of “pure channels” each of which contains only one type of cytological object. In the examples shown, channel purity was achieved by simple means. When more complex fluorophores with overlapping spectral bands are used, the use of spectral unmixing software would be necessary (Dickinson *et al.* 2001; Sinclair *et al.* 2004). The experiments shown here can be expanded to larger-scale studies. In future work, one can include larger numbers of channels describing more sets of structural and functional components. Although not demonstrated here, this approach, in

principle, allows combinatoric labeling and analysis of large numbers of such entities using a modest number of fluorophores. Recent advances such as quantum dots (Jaiswal *et al.* 2003) can be expected to further accelerate this potential.

The software strategy is driven by the availability of pure channels. By integrating separately developed 3-D image analysis tools for different types of cytological objects, it is possible to attempt a more detailed analysis of complex biological systems such as the neurovascular unit. This advance was made possible by integration of our diverse image analysis tools, especially high-quality blob and tube segmentation codes. By using key objects, especially the cell nuclei and the microvascular segments, as a spatial anchor/reference, it was possible to quantify a potentially unlimited number of fluorophore signals by association analysis. Indeed, combinatoric association analysis is the logical “glue” that serves as a powerful yet biologically meaningful integrative principle. The NVU example presented in this work represents the simplest instance of such analysis.

The resin casts of the neurovasculature provided a unique set of challenges for the image analysis software. The rhodamine B-doped resin displayed some heterogeneous stain distribution that made determination of initial seed points challenging. Blood vessels near the tissue face were frequently broken during sectioning, resulting in tubular fragments. Using local maxima as in our previous method of seed point detection produced seed points located close to vessel boundary rather than at the vessel centerline. By reformulating the seed point detection as a 1-D multi-scale matched-filter to detect known signals (as modeled by the generalized-cylinder model) in noise (Kay 1993), we are able to obtain the desired seed point placements. The tracing algorithms from prior work were adequate after this enhancement.

The vascular cast data sets used in this study presented a unique set of challenges for quantitation. Many of the values we obtained for blood vessel diameters were between 1 and 2 microns, smaller than the average 4-5 microns commonly reported in other casting studies (Hossler and Douglas 2001). These values are not likely due to difficulties in setting threshold values to recognize the entire vessel during analysis, since manual validation confirmed that the traced boundaries of vascular elements are reasonably accurate. Rather, these data seem to reflect a shortcoming in the vascular casting technique at

this time. Indeed, SEM analysis of corrosion casts using these same tissue samples has revealed that many of the smaller vessels are incompletely filled, often appearing collapsed (data not shown). Subsequent studies in our lab have identified changes to buffer composition and have led to pressure perfusion protocols that significantly improve cast quality. The ability of our analysis to identify a potential procedural issue that we could confirm using scanning electron microscopy underscores the strength of this technique.

Some of the observed nuclear undersegmentation may be due to the relatively large Z-step size used for this study. The 1 μ m steps were chosen instead of 0.375 μ m (which would match the X- and Y-resolution) because they appeared during image collection to provide adequate vertical resolution while reducing the effects of photobleaching, which were especially noticeable with the Nissl stain. In addition, HBHS was selected as a mounting media over glycerin in an attempt to avoid tissue shrinkage and preserve the relationship between tissue and the vascular cast, and to quickly transition to the aqueous alkaline solutions necessary to prepare corrosion casts. As a result, the tissue was not cleared, and fluorescence signal may have been scattered and attenuated more than usual. Data generated using more conventional techniques will likely generate fewer anomalies. We are currently developing tissue preparation and image analysis strategies to address these challenges.

The life-sciences researcher is often able to perform automated 2D image analysis using off-the-shelf software, e.g., NIH Image, MetaMorph by Universal Imaging and VoxeView by Vital Images. The sheer complexity and variability of biological imagery, and the current state of evolution of automated 3-D image analysis technology imply that the assistance of an image analysis specialist is often called for. It is hoped that the terminology and language presented here (blobs, tubes, clouds, etc.) can bridge these disciplines. The organization of image analysis by object types also forms a solid basis for facilitating productive discussion between life-sciences researchers and computer scientists.

Quantitative image analysis is a broadly applicable approach with specific benefits to investigations of the neurovascular unit. By facilitating the identification of different CNS cell types relative to one another and the neurovasculature, this software allows us to explore how these interactions change in

different brain regions and in response to disease or injury. The ability to characterize multiple biological elements with markedly different characteristics (e.g. tubes, clouds, blobs), while discriminating subtle differences in conserved features (blob classification) is essential to the study of the neurovascular unit.

5. LITERATURE CITED

- Abdul-Karim, M.-A., K. Al-Kofahi, et al. (2003). "Automated tracing and change analysis of angiogenic vasculature from in vivo multiphoton confocal image time series." Microvascular Research **66**(2): 113-125.
- Abu-Tarif and A. Ahmad (2002). Volumetric registration based on intensity and geometry features. PhD Thesis, Rensselaer Polytechnic Institute, Troy, NY.
- Adams, R. and L. Bischof (1994). "Seeded region growing." Pattern Analysis and Machine Intelligence, IEEE Transactions on **16**(6): 641-647.
- Adiga, P. S. U. and B. B. Chaudhuri (1999). "Efficient cell segmentation tool for confocal microscopy tissue images and quantitative evaluation of FISH signals." Microscopy Research and Technique **44**(1): 49-68.
- Adiga, U. and B. Chaudhuri (2001). "An efficient method based on watershed and rule-based merging for segmentation of 3D histo-pathological images." Pattern Recognition **34**: 1449-1458.
- Adiga, U. and B. Chaudhuri (2001). "Some efficient methods to correct confocal images for easy interpretation." Micron **32**(4): 363-70.
- Al-Kofahi, K. A., A. Can, et al. (2003). "Median-based robust algorithms for tracing neurons from noisy confocal microscope images." Information Technology in Biomedicine, IEEE Transactions on **7**(4): 302-317.
- Al-Kofahi, K. A., S. Lasek, et al. (2002). "Rapid automated three-dimensional tracing of neurons from confocal image stacks." Information Technology in Biomedicine, IEEE Transactions on **6**(2): 171-187.
- Al-Kofahi, O., A. Can, et al. (2002). Multi-View Three-Dimensional Image Montaging & Signal Attenuation Correction For Maximizing The Imaging Depth And Lateral Extent Of Confocal Microscopes. Microscopy and Microanalysis, Quebec.
- Ancin, H., B. Roysam, et al. (1996). "Advances in automated 3-D image analyses of cell populations imaged by confocal microscopy." Cytometry **25**(3): 221-34.
- Ballard, D. H. and C. M. Brown (1982). Computer vision. Englewood Cliffs, N.J., Prentice-Hall.
- Beck, J. C., J. A. Murray, et al. (2000). "Computer-assisted visualizations of neural networks: expanding the field of view using seamless confocal montaging." Journal of neuroscience methods **98**(2): 155-63.
- Becker, D. E., H. Ancin, et al. (1996). "Automated 3-D montage synthesis from laser-scanning confocal images: application to quantitative tissue-level cytological analysis." Cytometry : the journal of the Society for Analytical Cytology **25**(3): 235-45.
- Besl, P. J. and R. C. Jain (1988). "Segmentation through variable-order surface fitting." Pattern Analysis and Machine Intelligence, IEEE Transactions on **10**(2): 167-192.
- Black, M. J. and A. Rangarajan (1996). "On the Unification of Line Processes, Outlier Rejection, and Robust Statistics with Applications in Early Vision." International Journal of Computer Vision **19**(1): 57-91.
- Blake, A. and A. Zisserman (1987). Visual reconstruction. Cambridge, Mass., MIT Press.

- Borgefors, G. (1986). "Distance transformations in digital images." Comput. Vis., Graphics and Im. Prac. **34**: 344-371.
- Bovik, A. C., S. J. Aggarwal, et al. (2001). Automatic area and volume measurements from digital biomedical images. Image analysis : methods and applications. D.-P. Häder. Boca Raton, FL, CRC Press: 23-64.
- Can, A., O. Al-Kofahi, et al. (2003). "Attenuation correction in confocal laser microscopes: a novel two-view approach." J Microsc **211**(1): 67-79.
- Can, A., H. Shen, et al. (1999). "Rapid automated tracing and feature extraction from retinal fundus images using direct exploratory algorithms." Information Technology in Biomedicine, IEEE Transactions on **3**(2): 125-138.
- Can, A., C. V. Stewart, et al. (2002). "A feature-based, robust, hierarchical algorithm for registering pairs of images of the curved human retina." Pattern Analysis and Machine Intelligence, IEEE Transactions on **24**(3): 347-364.
- Castenholz, A. (1995). "Examination of injected specimens by confocal laser scanning microscopy and scanning electron microscopy." Scanning. Microsc. **9**: 1245-1254.
- Castleman, K. (1996). Digital image processing, Prentice-Hall.
- Castleman, K. R. and B. S. White (2001). "Dot count proportion estimation in FISH specimens." Bioimaging **3**(2): 88-93.
- Chawla, M. K., G. Lin, et al. (2004). "3D-catFISH: a system for automated quantitative three-dimensional compartmental analysis of temporal gene transcription activity imaged by fluorescence in situ hybridization." Journal of Neuroscience Methods **139**(1): 13-24.
- Cohen, A. R., B. Roysam, et al. (1994). "Automated tracing and volume measurements of neurons from 3-D confocal fluorescence microscopy data." Journal of microscopy **173**(Pt 2): 103-14.
- Cox, S., T. Woolsey, et al. (1993). "Localized dynamic changes in cortical blood flow with whisker stimulation corresponds to matched vascular and neuronal architecture of rat barrels." J. Cereb Blood Flow Metab **13**(6): 899-913.
- del Zoppo, G. (1994). "Microvascular changes during cerebral ischemia and reperfusion." Cerebrovasc Brain Metab Rev. **6**(1): 47-96.
- del Zoppo, G. and T. Mabuchi (2003). "Cerebral microvessel responses to focal ischemia." J Cereb Blood Flow Metab. **23**(8): 879-894.
- Diaspro, A. (2002). Confocal and two-photon microscopy : foundations, applications, and advances. New York, Wiley-Liss.
- Dickinson, M., G. Bearman, et al. (2001). "Multi-Spectral Imaging and Linear Unmixing Add a Whole New Dimension to Laser Scanning Fluorescence Microscopy." BioTechniques **31**(6): 1272-1278.
- Guigues, L., H. Le Men, et al. (2003). "The hierarchy of the cocoons of a graph and its application to image segmentation." Pattern Recognition Letters **24**(8): 1059-1066.
- He, W., T. A. Hamilton, et al. (2003). "Automated three-dimensional tracing of neurons in confocal and brightfield images." Microscopy and microanalysis : the official journal of Microscopy Society of America, Microbeam Analysis Society, Microscopical Society of Canada **9**(4): 296-310.
- Hossler, F. and J. Douglas (2001). "Vascular Corrosion Casting: Review of Advantages and Limitations in the Application of Some Simple Quantitative Methods." Microsc Microanal. **7**(3): 253-264.
- Huber, P. J. (1981). Robust statistics. New York, Wiley.
- Jaiswal, J. K., H. Mattoussi, et al. (2003). "Long-term multiple color imaging of live cells using quantum dot bioconjugates." Nat Biotechnol **21**(1): 47-51.

- Kay, S. M. (1993). Fundamentals of statistical signal processing. Englewood Cliffs, N.J., Prentice-Hall PTR.
- Kitano, H. (2002). "Systems biology: a brief overview." Science **295**(5560): 1662-4.
- Koh, I. Y., W. B. Lindquist, et al. (2002). "An image analysis algorithm for dendritic spines." Neural computation **14**(6): 1283-310.
- Kohane, I. S., A. T. Kho, et al. (2003). Microarrays for an integrative genomics. Cambridge, Mass, MIT Press.
- Lin, G., U. Adiga, et al. (2003). "A hybrid 3D watershed algorithm incorporating gradient cues and object models for automatic segmentation of nuclei in confocal image stacks." Cytometry **56A**(1): 23-36.
- Lin, G., M. K. Chawla, et al. (2004). "Hierarchical, model-based merging of multiple fragments for 3-D segmentation of nuclei." Cytometry **62**(2): DOI: 10.1002/cyto.a.20099.
- Mahadevan, V., H. Narasimha-Iyer, et al. (2004). "Robust model-based vasculature detection in noisy biomedical images." Information Technology in Biomedicine, IEEE Transactions on **8**(3): 360-376.
- Malpica, N., C. O. de Solorzano, et al. (1997). "Applying watershed algorithms to the segmentation of clustered nuclei." Cytometry **28**(4): 289-97.
- Matsumoto, B. and B. American Society for Cell (2002). Cell biological applications of confocal microscopy. Amsterdam ; London, Academic Press.
- Meijering, E., M. Jacob, et al. (2004). "Design and validation of a tool for neurite tracing and analysis in fluorescence microscopy images." Cytometry **58A**(2): 167-76.
- Nedergaard, M., B. Ransom, et al. (2003). "New roles for astrocytes: redefining the functional architecture of the brain." Trends Neurosci. **26**(10): 523-530.
- Netten, H., I. T. Young, et al. (1997). "FISH and chips: Automation of fluorescent dot counting in interphase cell nuclei." Cytometry **28**(1): 1-10.
- Neumann, A. (2003). "Graphical Gaussian shape models and their application to image segmentation." Pattern Analysis and Machine Intelligence, IEEE Transactions on **25**(3): 316-329.
- Newman, E. A. (2003). "New roles for astrocytes: Regulation of synaptic transmission." Trends in Neurosciences **26**(10): 536-542.
- Olson, K. (1985). "Preparation of fish tissues for electron microscopy." J. Electron Microsc. Tech. **2**: 217-228.
- Park, J., K. Choi, et al. (2003). "Coordinated interaction of the vascular and nervous systems: from molecule- to cell-based approaches." Biochem Biophys Res Commun. **311**(2): 247-253.
- Pawley, J. B. (1995). Handbook of biological confocal microscopy. New York, Plenum Press.
- Russ, J. C. (1994). The image processing handbook. Boca Raton, CRC Press.
- Sato, Y., S. Nakajima, et al. (1998). "Three-dimensional multi-scale line filter for segmentation and visualization of curvilinear structures in medical images." Medical image analysis **2**(2): 143-68.
- Serra, J. P. and P. Soille (1994). Mathematical morphology and its applications to image processing. Dordrecht ; Boston, Kluwer Academic Publishers.
- Shapiro, H. M. (2003). Practical flow cytometry. New York ; [Great Britain], Wiley-Liss.
- Sheppard, C., D. Shotton, et al. (1997). Confocal laser scanning microscopy. Oxford, UK BIOS Scientific Publishers ; New York, NY, USA, Springer.
- Shi, J. and J. Malik (2000). "Normalized cuts and image segmentation." Pattern Analysis and Machine Intelligence, IEEE Transactions on **22**(8): 888-905.

- Simard, M., G. Arcuino, et al. (2003). "Signaling at the gliovascular interface." J Neurosci. **23**(27): 9254-9262.
- Sinclair, M. B., J. A. Timlin, et al. (2004). "Design, Construction, Characterization, and Application of a Hyperspectral Microarray Scanner." Applied Optics **43**(10): 2079-2088.
- Solorzano, C. and E. Rodriguez (1999). "Segmentation of confocal microscope images of cell nuclei in thick tissue sections." Journal of Microscopy **193**(3): 212-226.
- Solórzano, C. O. d., A. Santos, et al. (1998). "Automated FISH spot counting in interphase nuclei: Statistical validation and data correction." Cytometry **31**(2): 93-99.
- Sun, Y., R. J. Lucariello, et al. (1995). "Directional low-pass filtering for improved accuracy and reproducibility of stenosis quantification in coronary arteriograms." Medical Imaging, IEEE Transactions on **14**(2): 242-248.
- Sunil Kumar, K. and U. B. Desai (1999). "Joint segmentation and image interpretation." Pattern Recognition **32**(4): 577-589.
- Trucco, E. and R. B. Fisher (1995). "Experiments in curvature-based segmentation of range data." Pattern Analysis and Machine Intelligence, IEEE Transactions on **17**(2): 177-182.
- Valeur, B. (2002). Molecular fluorescence : principles and applications. Weinheim ; New York, Wiley-VCH.
- Vincent, L. and P. Soille (1991). "Watersheds in digital spaces: an efficient algorithm based on immersion simulations." IEEE Trans On PAMI **3**(6).
- Weichert, F., H. Müller, et al. (2003). "Virtual 3D IVUS vessel model for intravascular brachytherapy planning. I. 3D segmentation, reconstruction, and visualization of coronary artery architecture and orientation." Medical physics **30**(9): 2530-6.
- Woolsey, T., C. Rovainen, et al. (1996). "Neuronal units linked to microvascular modules in cerebral cortex: response elements for imaging the brain." Cereb Cortex **6**(5).
- Wu, X. (1993). "Adaptive Split-and-Merge segmentation based on piecewise least-square approximation." IEEE Transactions on Pattern Analysis and Machine Intelligence **15**(8): 808-815.
- Xu, Y. and E. C. Uberbacher (1997). "2D image segmentation using minimum spanning trees." Image and Vision Computing **15**(1): 47-57.
- Yoder, E. (2002). "Modifications in astrocyte morphology and calcium signaling induced by a brain capillary endothelial cell line." Glia, **38**(2): 137-145.
- Zhu, S. C. and A. Yuille (1996). "Region competition: unifying snakes, region growing, and Bayes/MDL for multiband image segmentation." Pattern Analysis and Machine Intelligence, IEEE Transactions on **18**(9): 884-900.
- Zimmermann, T., J. Rietdorf, et al. (2002). "Spectral imaging and linear un-mixing enables improved FRET efficiency with a novel GFP2-YFP FRET pair." FEBS Lett **531**(2): 245-9.
- Zimmermann, T., J. Rietdorf, et al. (2003). "Spectral imaging and its applications in live cell microscopy." FEBS Lett **546**(1): 87-92.
- Zonta, M., M. Angulo, et al. (2003). "Neuron-to-astrocyte signaling is central to the dynamic control of brain microcirculation." Nat Neurosci. **6**(1): 43-50.
- Zucker, S. W. (1976). "Region growing: Childhood and adolescence." Computer Vision, Graphics and Image Processing **5**: 382-399.

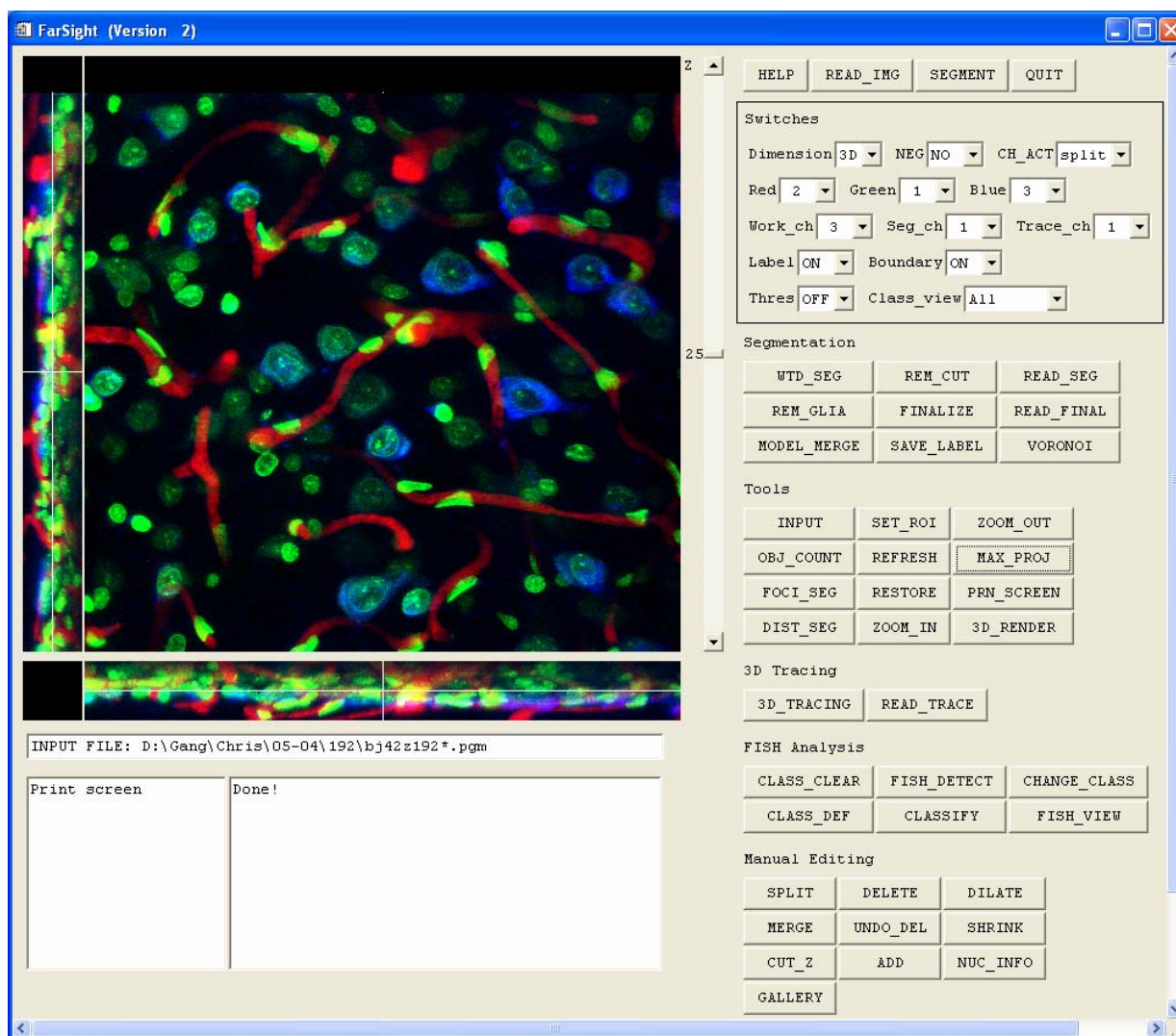


Figure 1: A screen view of the integrative software system showing a sample triple-label dataset displayed as a set of three projections (x - y , y - z , and x - z). Cell nuclei (blob-like objects) are shown in green. Blood vessels (tube-like objects) are shown in red, and the unstructured cloud-like object in the third channel (blue) is the Nissl cytoplasmic stain. Notice that three general blob morphologies can be distinguished: larger, dimmer, and more heterogenous neuronal nuclei; smaller, brighter and more uniform glia; and flat, intense endothelial cells. Differences in cloud shape and volume can also be used to distinguish larger pyramidal neurons from other neuron types.

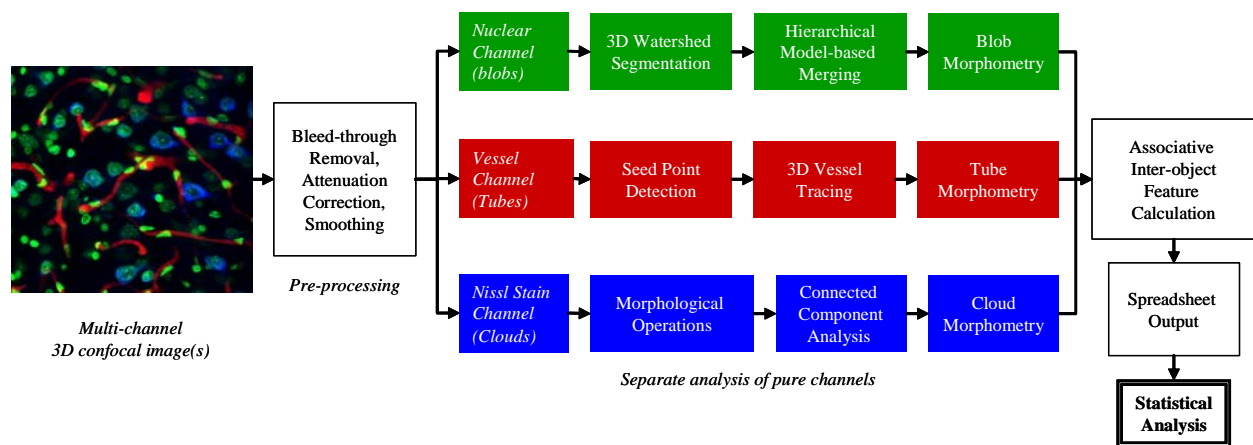


Figure 2: Illustrating the main steps for automated analysis of multi-channel 3-D confocal image stacks containing different object classes. The separate imaging of cytological objects in different channels enables a “divide and conquer” approach to the analysis of such complex systems. Only the main steps in the analysis of each pure channel are noted in this simplified diagram. The details are described in other cited papers.

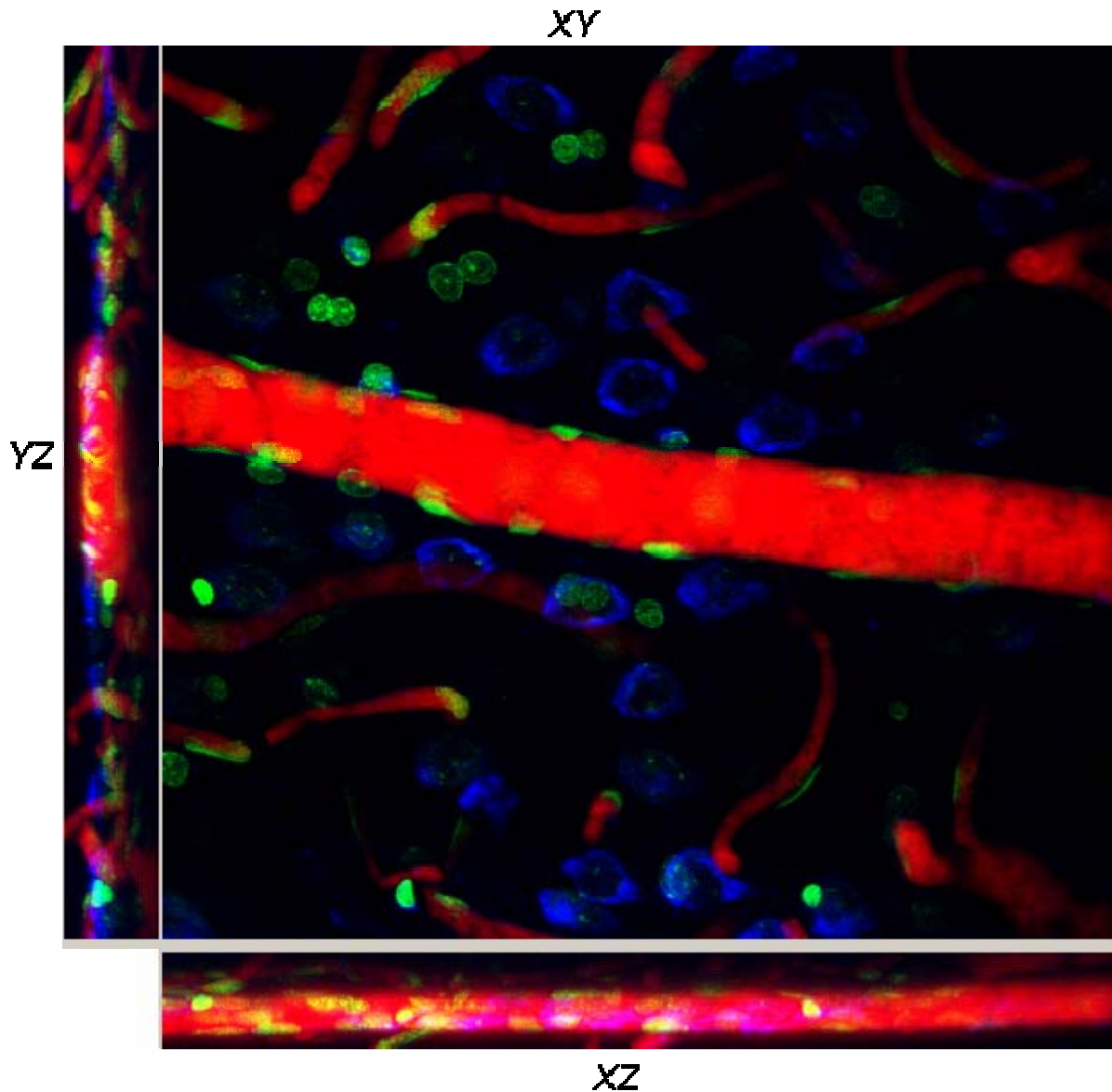


Figure 3: Sample image illustrating the need for image pre-processing to overcome common sources of variability especially: non-uniform staining, such as the nuclei in the left portion of the image appearing brighter than in the right portion; and apparent discontinuities in the microvasculature; depth-dependent attenuation making deeper vessels appearing dimmer than others; and unequal depth-dependent attenuation of the fluorescent channels. Nuclear staining in different cell types appears non-uniform due to differences in the distribution of DNA content, and nuclear volume varies according to cell structure and activity, as evidenced by the dim, diffuse neuronal nuclei surrounded by Nissl stain, and also due to variable attenuation. Variations in object volume, intensity and shape are not only challenging for image analysis, but also a means of categorizing different cell types.

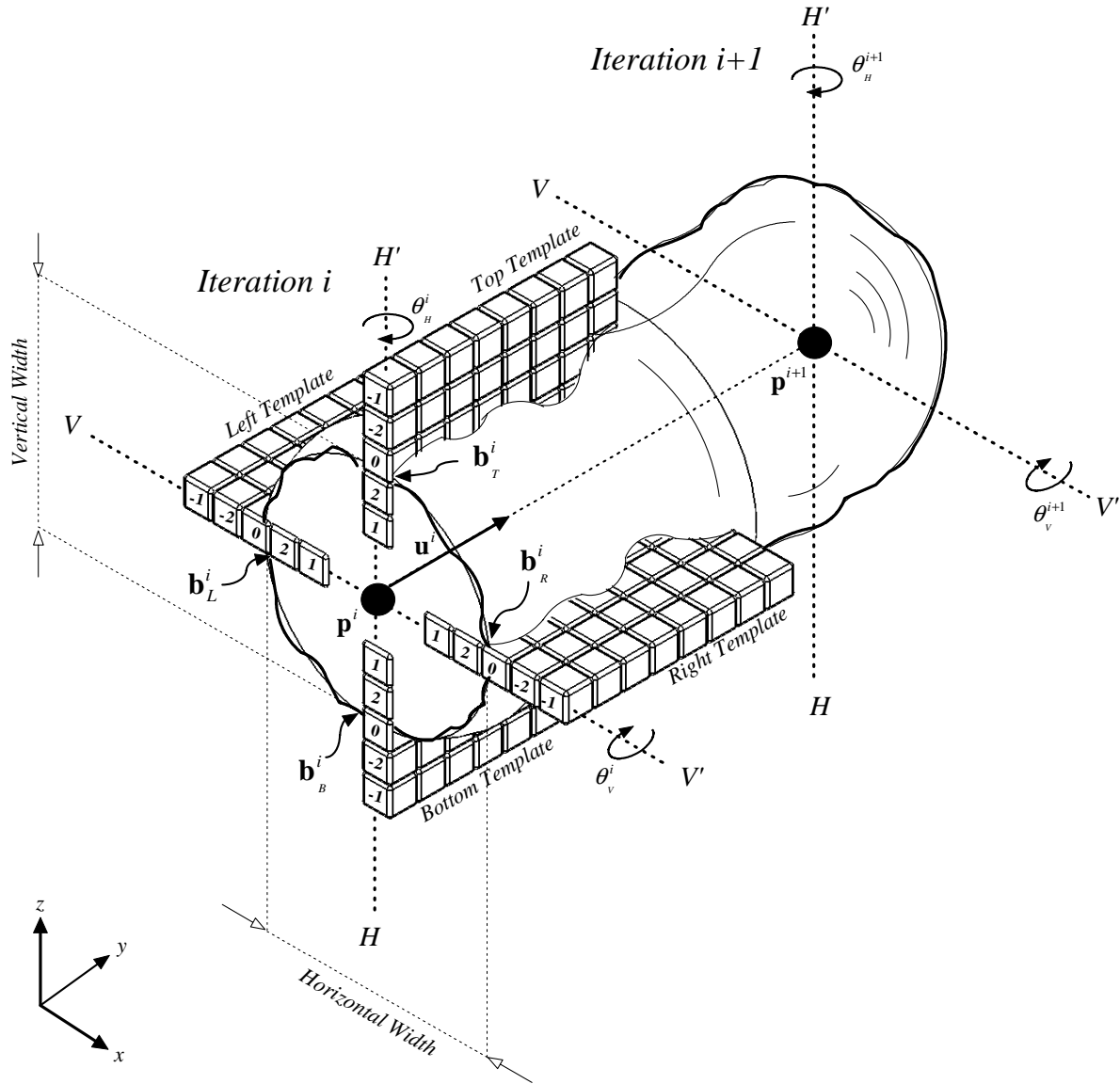
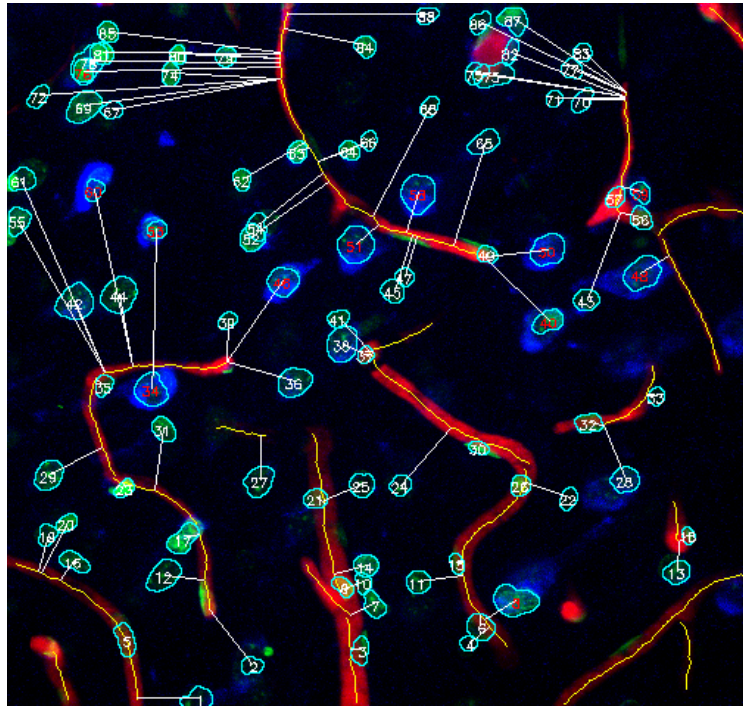
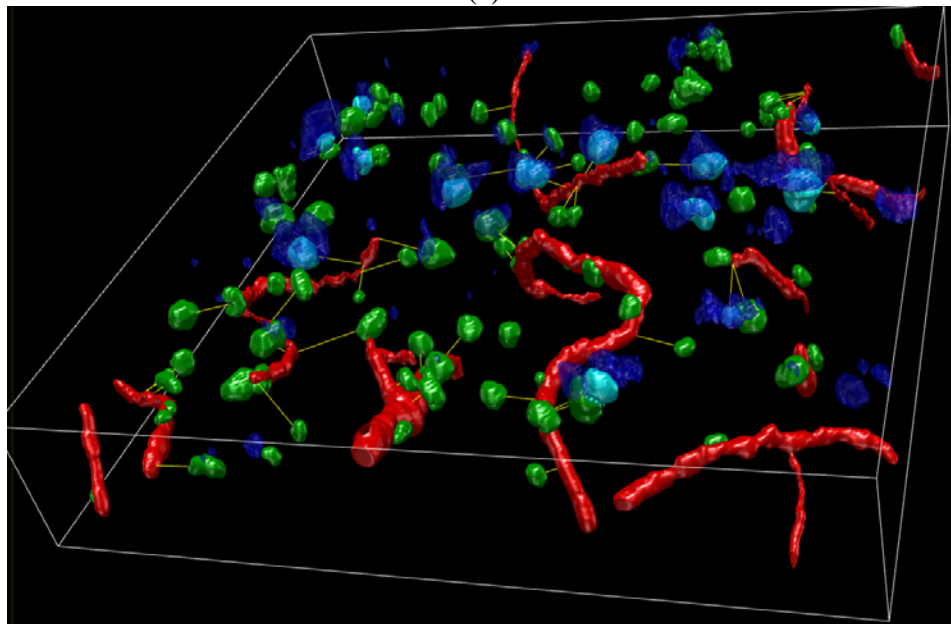


Figure 4: Illustrating the generalized cylinder modeling of the tube-like microvasculature, mathematical notation, and the templates for automated 3-D tracing. Robustness to irregularities of the object boundary relative to the straight-boundary assumption is achieved by use of the median template response.



(a)



(b)

Figure 5: Illustrating intra- and inter-object measurements. (a) Nuclei are outlined in white, and numbered in white (class ‘0’; non-neuronal) or red (class ‘1’; neuronal). The vessel centerline traces are shown in yellow. The distance from each nucleus to the nearest vessel is indicated by a white line. Nuclei that are closer to an edge of the image than they are to the nearest vessel are excluded. (b) Sample 3-D graphical rendering of the same data allows improved visualization by perspective, and interactive manipulation of viewpoint.

Table 1: A partial tabular output corresponding to Figure 5. Standard nuclear features such as 3-D location, average intensity, volume, texture and shape factor; and associative inter-object features such as the distance of each nucleus to the vasculature. The nuclear classification result is shown by the “Class” column, where ‘1’ and ‘0’ stand for nuclei with and without the Nissl stain, respectively. The (x, y, z, volume) measurements are in voxel units. The distances to vessels and vessel diameters are in μm .

Nuclear ID	X	Y	Z	Intensity	Volume	Texture	Shape Factor	Class	Nissl Volume	Distance to vessel	Vessel diameter
1	122	13	25	9	350	4.12	0.70	0	0	72.86	4.24
2	75	20	14	52	655	14.02	0.77	0	0	35.61	4.24
3	272	22	17	34	1430	22.67	0.80	0	0	27.95	16.53
4	243	25	36	14	681	8.06	0.68	0	0	13.82	10.82
5	137	35	21	9	640	7.79	0.79	0	0	76.58	4.24
6	301	36	13	80	1473	39.17	0.81	0	0	14.25	12.10
7	177	38	9	25	1934	25.42	0.81	0	0	67.19	10.82
8	348	43	15	16	344	9.73	0.68	0	0	4.43	16.28
9	233	44	24	14	1290	12.46	0.74	0	0	19.07	8.36
10	17	45	11	22	1518	20.79	0.77	0	0	20.43	6.08
11	433	64	11	27	1141	16.36	0.73	0	0	8.22	4.26
12	374	69	18	9	557	7.68	0.75	0	0	34.37	5.66
13	109	71	6	27	2169	19.58	0.73	1	6084	49.02	4.24
14	406	80	15	60	378	13.19	0.71	0	0	2.88	3.61
15	449	82	12	41	534	16.47	0.70	0	0	27.34	3.61

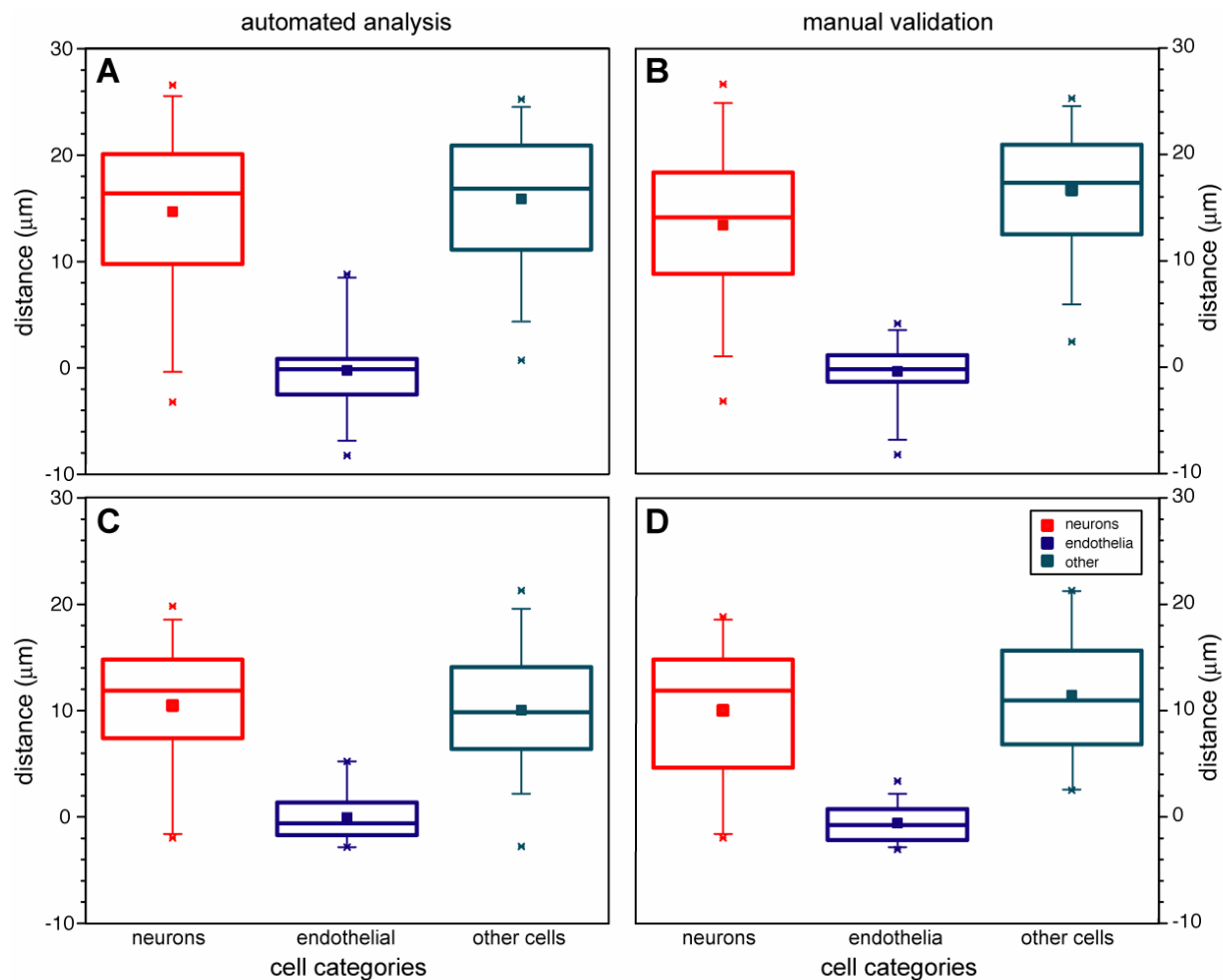


Figure 6: Validation of automated measurements for descriptions of cell distributions around vasculature elements in rat neocortex. Data obtained by automated analyses (A & C) demonstrate measured distances between neurons (blue graphic elements), endothelial cells (green graphic elements), and other cells (red graphic elements). Data validated by manual inspection of individual optical sections (B & D) for each data set demonstrate the accuracy of the automated analysis. These are representative of data sets collected from two of eight randomly selected samples from rat cortex. Neuronal nuclei were identified because of their close association with Nissl-stained clouds. Endothelial cell nuclei were identified by their close apposition to vascular elements. The “other cells” category includes all cells for which there were not sufficient criteria for categorization, e.g. astrocytes, microglial, and neuronal nuclei that did stain with Nissl. From top to bottom of each column of data the symbols represent: maximum data value (x), 95th percentile (top of line), 75th percentile (top of box), median (line), mean (square), 25th percentile (bottom of box), 5th percentile (bottom of line), minimum data value (x). The numbers of nuclei included in this analysis were for neurons (21, 19, 24, 39), endothelia (25, 21, 36, 56), and other cells (33, 33, 60, 76), A, B, C, and D, respectively.

